Synthesis, structural insights, antimicrobial and cytotoxic potentials of Mn(II) and Fe(III) complexes with a novel Triazine–Quinoline ligand

Inorganica Chimica Acta 595 (2026) 123114

Contents lists available at ScienceDirect

Inorganica Chimica Acta

journal homepage: www.elsevier.com/locate/ica

Synthesis, structural insights, antimicrobial and cytotoxic potentials of Mn(II) and Fe(III) complexes with a novel Triazine–Quinoline ligand

Amal Yousri [a], Esraa Alaa [a], Francoise M. Amombo Noa [b,*], Lars Öhrström [b,*], Ayman El-Faham [a,c], Morsy A.M. Abu-Youssef [a], Saied M. Soliman [a,*], Eman M. Fathalla [a], Sara M. Khattab [a]

[a] Department of Chemistry, Faculty of Science, Alexandria University, P.O. Box 426, Ibrahimia, Alexandria 21321, Egypt
[b] Department of Chemistry and Chemical Engineering, Chalmers University of Technology, SE-41296 Gothenburg, Sweden
[c] Department of Basic Medical Sciences, College of Medicine, Dar Al Uloom University, P. O. Box 45142, Riyadh 11512, Saudi Arabia

ARTICLE INFO

Keywords:
d^5 metal complexes
X-ray crystal structure
Hirshfeld
AIM studies
Cytotoxicity
Antimicrobial

ABSTRACT

Two novel Mn(II) and Fe(III) complexes were synthesized using a newly developed *s*-triazine ligand, *N*-(4,6-*bis*(3,5-dimethyl-1*H*-pyrazol-1-yl)-1,3,5-triazin-2-yl)quinolin-8-amine, and their structures were fully confirmed using single-crystal X-ray diffraction. The Mn(II) ion is penta-coordinated with one *NNN*-tridentate chelate and two chloride ions leading to the $[MnLCl_2]$ formula for **1**. The $[Fe_2L_2(\mu\text{-}O)(H_2O)_4](NO_3)_4.3H_2O$ comprised two hexacoordinated Fe(III) centers connected by an oxo bridge where each metal center is further coordinated with one *NNN*-tridentate chelate **L** and two water molecules. Hirshfeld analysis disclosed the highest contributing intermolecular interactions in the crystal of **1** to be H···H (43.3%), Cl···H (20.7%), and C···H (11.3%). For **2**, the main contributions are H···H (39.7 and 40.3%), O···H (33.6 and 32.0%), and H···C (16.0 and 15.9%), for units **A** and **B**, respectively. Atoms in molecules (AIM) analysis indicates that the Mn–N, Fe–N, and terminal Fe–O bonds are predominantly closed-shell in nature, while modest covalent character is observed for the Mn–Cl and bridging Fe–O bonds. Moreover, **1** and **2** exhibited enhanced anticancer activities than the free ligand **L** against HCT-116 and A-549 cancer cell lines, where **2** being the most potent (IC_{50} values of 9.05 ± 0.21 and 10.67 ± 0.25 μM, respectively). Compared to *cis*-platin, **1** and **2** demonstrated greater cytotoxic effects against HCT-116 cells (~1.2- and 3.1-fold, respectively). Additionally, the free ligand exhibited the strongest antimicrobial activity against *B. subtilis* and *C. albicans* with inhibition zone diameters (IZDs) of 18 and 11 mm, respectively, while **2** is more effective against *P.vulgaris,* with an IZD of 15 mm.

1. Introduction

Heterocyclic compounds have attracted significant interest due to their broad biological relevance [1]. Ligand systems containing heterocyclic structures are capable of forming metal chelates that exhibit a wide range of properties, including biological activity, catalytic functions, and potential applications in sensing technologies [1].

One of the most relevant heterocycles in modern medicinal chemistry is triazines, which are widely used in biopharmaceutical, textile, synthetic resin and rubber industries. They are also used in the manufacture of insecticides, tints, brightening agents, explosives, and surface-active agents [2]. 1,3,5-Triazine (commonly known as *s*-triazine) and its derivatives are widely recognized for their varied pharmacological activities, including bactericidal, virucidal, and anti-swelling effects, and have shown potential efficacy in antineoplastic, anti-leukemic, and antiretroviral therapies [3]. Furthermore, a wide range of triazine-based analogues have been utilized as central scaffolds in the design and synthesis of multisite ligand systems [4].

The nitrogen atoms in the triazine ring have lone pairs that can participate in coordination and hydrogen bonding interactions [5]. Additionally, its heteroaromatic π-electrons and rigid ring structure make it well suited for a variety of supramolecular interactions, including π-π stacking, anion-π, and electron-rich π interactions [5,6]. *s*-Triazine serves as a promising scaffold for the development of bioactive compounds with reduced toxicity and is frequently used by researchers to design effective drug-like molecules [7].

* Corresponding authors.
E-mail addresses: mystere@chalmers.se (F.M. Amombo Noa), ohrstrom@chalmers.se (L. Öhrström), ayman.a@dau.edu.sa (A. El-Faham), morsy5@alexu.edu.eg (M.A.M. Abu-Youssef), saied1soliman@yahoo.com (S.M. Soliman), Eman.nomeir@alexu.edu.eg (E.M. Fathalla), SaraMahmoud@alexu.edu.eg (S.M. Khattab).

https://doi.org/10.1016/j.ica.2026.123114
Received 6 November 2025; Received in revised form 15 January 2026; Accepted 4 February 2026
Available online 6 February 2026

The rational design of chemical compounds guided by structure-activity relationship analysis has driven the development of more effective, less toxic, and highly selective pharmaceutical agents [8]. Apart from their application as bioactive scaffolds and in therapeutic chemistry, *s*-triazine and its derivatives have demonstrated considerable utility in organic synthesis, formulation of high-energy materials, and construction of advanced functional architectures such as dendrimers and supra-molecular aggregates [5,9–11]. The *s*-triazine framework has played a pivotal role in the synthesis of bioactive molecules with reduced toxicity profiles and has been used in the development of dendrimers constructed from melamine (2,4,6-triamino-*s*-triazine), which are utilized in cancer treatment and various biomedical therapeutic strategies [11].

Numerous pyrazolyl derivatives have attracted considerable attention due to their promising role as ligands in diverse biological, analytical, and pharmacological applications [12]. Furthermore, many of these compounds exhibit notable anticancer and antimicrobial properties [13–16]. Certain triazine-pyrazole conjugates have been evaluated and recognized as potential inhibitors of the photosynthetic electron transport chain [17]. In parallel, quinoline-based derivatives which are known for their broad pharmacological properties, have demonstrated strong antibacterial efficacy against both Gram-negative and Gram-positive bacterial strains [18]. Notably, quinoline is considered an important biologically active moiety with numerous biological properties, such as antibacterial, anti-inflammatory, and antidepressant effects [19–21].

On the other hand, metal ions are essential in biology due to their significant roles in therapeutic and diagnostic applications. Their distinctive properties, such as redox versatility, flexible coordination behavior, and ability to interact with organic substrates significantly enhance their applicability in both biomedical research and therapeutic development [22]. Specifically, manganese is an essential nutrient that plays a crucial role in numerous metabolic activities. Manganese is involved in supporting normal development, activating metalloenzymes, contributing to energy production, regulating immune and neurological functions, modulating reproductive hormones, and providing antioxidant defense against free radical-induced damage [23,24]. Also, it supports the proper synthesis and secretion of insulin [25]. Moreover, manganese complexes are gaining significance in biomedical applications, such as superoxide dismutase mimetics [26,27], magnetic resonance imaging (MRI) contrast agents [28,29], and chelation therapies for manganese overload [30]. Furthermore, manganese is successfully associated with high kinetic inertness, strong stability, and selective binding properties of its complexes [31].

Besides, iron is one of the most abundant elements in the environment. Iron and its complexes participate in a variety of critical biochemical processes, such as RNA synthesis, energy production, photosynthesis, nitrogen fixation, oxygen transport, and oxygenation [32]. Iron complexes exhibit a wide range of catalytic, anticancer, and antimicrobial actions [33,34]. Hence, these complexes are known for their ability to cause DNA damage [35]. Consequently, iron complexes have attracted considerable attention in medicinal chemistry due to their role in redox-regulated cellular processes and selective interactions with DNA and proteins, whereas iron is an essential, tightly controlled bio-metal crucial for cancer cell proliferation [30]. Iron(III) typically forms hexacoordinate, high spin, and kinetically labile complexes, except when coordinated with strong field ligands or macrocyclic ligands [36]. Moreover, several iron(III) complexes have been extensively investigated and employed as contrast agents in magnetic resonance imaging [37].

As an extension of previous analyses concerning the distinctive structural motifs and significant biological potential of *s*-triazine derivatives and their metal complexes, this work reports the design, synthesis, and comprehensive evaluation of new Mn(II) and Fe(III) complexes with *N*-(4,6-*bis*(3,5-dimethyl-1*H*-pyrazol-1-yl)-1,3,5-triazin-2-yl)quinolin-8-amine; **L**. The new complexes were characterized using elemental analysis, FT-IR, UV–Vis, single crystal X-ray diffraction, and powder X-ray diffraction (PXRD). The biological activities of the new complexes were also investigated in comparison to their free ligand **L**.

2. Experimental

2.1. Materials and methods

Information regarding the chemicals, instrumentation, and methods used for spectroscopic analyses are provided in supplementary data.

2.2. Syntheses of the studied compounds

2.2.1. Synthesis of *L*

The synthetic strategy commenced with the regioselective nucleophilic aromatic substitution of cyanuric chloride, wherein one chlorine atom was selectively displaced by 8-aminoquinoline, an aromatic nitrogen-based nucleophile. This reaction was facilitated by sodium hydrogen carbonate, which acted as a scavenger for the released of hydrogen chloride, in accordance with previously established protocols [38]. To ensure selective substitution of only one chlorine atom, the reaction was optimized by maintaining the temperature at 0 °C, which allowed the two remaining chlorine atoms on the triazine ring to stay intact, yielding *N*-(4,6-dichloro-1,3,5-triazin-2-yl)quinolin-8-amine. This intermediate subsequently reacted with 80% hydrazine hydrate in ethanol under reflux conditions overnight, leading to the formation of *N*-(4,6-dihydrazineyl-1,3,5-triazin-2-yl)quinolin-8-amine. Without purification, the crude hydrazine derivative was further reacted with acetylacetone in the presence of 20% acetic acid-ethanol mixture as the reaction medium, following the methodologies previously reported in the literature [39,40], thereby affording the target compound *N*-(4,6-*bis*(3,5-dimethyl-1*H*-pyrazol-1-yl)-1,3,5-triazin-2-yl)quinolin-8-amine, as supported by the spectral data provided in supplementary data. IR (KBr, cm^{-1}): 3250 $\nu_{(N-H)}$, 3074 $\nu_{(C-H)}$, 2927 $\nu_{(C-H)}$, 1647 $\nu_{(C=N)}$, 1581 $\nu_{(C=C)}$, 1480 $\nu_{(C=C)}$ (**Fig. S1**, Supplementary data). ^{1}H NMR ($CDCl_3$) δ: 2.36 (s, 6H, $2CH_3$), 2.77 (s, 6H, $2CH_3$), 6.07 (s, 2H, $2CH_{pyr}$), 7.49–7.60 (m, 3H, CHar), 8.20 (d, 1H, 1CHar), 8.79–8.85 (m, 2H, CHar), 10.20 (s, 1H, NH) ppm (**Fig. S2**) and ^{13}C NMR ($CDCl_3$-d_6) δ: 13.9,16.0, 111.6, 117.9, 121.9, 122.1, 127.1, 128.3, 133.9, 136.8, 138.6, 148.4, 152.8, 165.0 ppm (**Fig. S3**).

2.2.2. Syntheses of complexes *1* and *2*

1 and **2** were synthesized by mixing 10 mL of an ethanolic solution of **L** (0.3 mmol; 123.4 mg) with either 10 mL of an ethanolic solution of $MnCl_2{\cdot}4H_2O$ (0.3 mmol; 59.4 mg) or $Fe(NO_3)_3{\cdot}9H_2O$ (0.3 mmol; 121.2 mg), respectively. Upon mixing, the solution of **1** immediately became turbid, which was then dissolved by heating the mixture, followed by filtration. For **2**, the reddish-brown turbidity was dissolved by adding distilled water, resulting in a clear solution. The clear solutions were left to evaporate slowly at room temperature for a couple of days. Dark brown crystals of **1** and reddish-brown crystals of **2** were formed after five and seven days, respectively.

[$MnLCl_2$] Yield; 78%. $C_{22}H_{21}Cl_2MnN_9$; Anal. Calc. C, 49.18; H, 3.94; N, 23.46; Mn, 10.22; Found: C, 49.07; H, 3.93; N, 23.37; Mn, 10.13. IR (KBr, cm^{-1}): 3261 $\nu_{(N-H)}$, 3057 $\nu_{(C-H)}$, 2925 $\nu_{(C-H)}$, 1585 $\nu_{(C=N)}$, 1534 $\nu_{(C=C)}$, 1484 $\nu_{(C=C)}$ (**Fig. S4**).

[$Fe_2L_2(\mu$-$O)(H_2O)_4](NO_3)_4{\cdot}3H_2O$ Yield; 80%. $C_{88}H_{115}Fe_4N_{44}O_{41.5}$; Anal. Calc. C, 39.49; H, 4.33; N, 23.03; Fe, 8.35; Found: C, 39.38; H,4.32; N, 22.92; Fe, 8.26. IR (KBr, cm^{-1}): 3431 $\nu_{(O-H)}$, 3102 $\nu_{(C-H)}$, 2927 $\nu_{(C-H)}$, 1630 $\nu_{(C=N)}$, 1538 $\nu_{(C=C)}$, 1488 $\nu_{(C=C)}$, 1383 $\nu_{as(N-O)}$, 1043 $\nu_{s(N-O)}$ (**Fig. S5**).

2.3. X-ray structure determination

Data collection of suitable single crystals of **1** and **2** were conducted on a Rigaku XtaL AB Synergy-DW diffractometer equipped with a HyPix-

Arc 150^0 detector using CuKα radiation (λ = 1.54184 Å) [41,42]. The diffraction data were acquired and processed with CrysAlisPro software package. Direct methods were utilized for both complexes (**1** and **2**) and the refinements were established by full-matrix least squares with SHELX-2018/3 [43] using Olex2 [44] software. The molecular and packing diagrams were generated using Mercury 2024.3.1 (Build 428,097), developed by the Cambridge Crystallographic Data Centre (CCDC) [45]. Some of the solvent molecules in **2** are disordered so the Mask command embedded in the Olex2 software was utilized to estimate the ratio of each solvent by the number of electrons based on the asymmetric unit (ASU). Both chlorine atoms in **1** are disordered and the modelling and disorder tools (embedded in Olex2) were employed to split the disordered chlorine atoms to suitable chemical occupancies. CCDC numbers 2,475,622 & 2,475,623.

2.4. Powder X-ray diffraction (PXRD)

Data collection of powder samples of **1** and **2** were done on a Rigaku XtaL AB Synergy-DW diffractometer equipped with a HyPix-Arc 150^0 detector using CuKα radiation (λ = 1.54184 Å) [40,41]. The diffraction data was acquired and processed with CrysAlisPro software package and the PXRD patterns are shown in **Fig. S6**.

2.5. Hirshfeld analysis

Hirshfeld analysis of molecular packing was performed using crystal explorer 21.5 program [46,47].

2.6. Computational studies

The AIM topological analysis was carried out using B3LYP method, as implemented in Gaussian 09 [48]. A mixed basis set was employed, wherein the 6-31G(d,p) was applied to non-metal atoms and LANL2DZ was used for metal centers [49]. The AIM parameters were subsequently evaluated using the Multiwfn 3.6.1 program [50].

2.7. Biological evaluation

The procedures employed for the evaluation of anticancer [51–53] and antimicrobial activities [54–57] were comprehensively detailed in Methods S1 and S2.

3. Results and discussion

3.1. Syntheses and characterization

The synthetic route for the target ligand is illustrated in (Scheme 1). The scheme was initiated with the preparation of *N*-(4,6-dichloro-1,3,5-triazin-2-yl) quinolin-8-amine, which was subsequently converted into *N*-(4,6-dihydrazineyl-1,3,5-triazin-2-yl)quinolin-8-amine, following established literature protocols [38–40]. The target pincer ligand *N*-(4,6-*bis*(3,5-dimethyl-1*H*-pyrazol-1-yl)-1,3,5-triazin-2-yl)quinolin-8-amine (**L**) was synthesized by adding acetylacetone in the presence of 20% acetic acid-ethanol mixture. A mononuclear Mn(II) and a dinuclear Fe(III) complexes based on *s*-triazine ligand were synthesized by self-assembly technique (**Scheme S1**). Their structures were confirmed by elemental analysis, UV–Vis, FT-IR, single X-ray crystal diffraction and PXRD. The $\nu_{(N-H)}$ stretching vibrations appeared at 3250 and 3261 cm^{-1} for **L** and **1**, respectively. In **2**, a broad band appeared at 3431 cm^{-1}, attributed to O–H stretching, which confirmed the presence of water molecules, which obscured the $\nu_{(N-H)}$ band. The aromatic $\nu_{(C-H)}$ sp^2 bands were detected at 3074, 3057, and 3102 cm^{-1}, respectively. Furthermore, the aliphatic $\nu_{(C-H)}$ bands were observed at 2927, 2925, and 2927 cm^{-1}, respectively. Both $\nu_{(C=N)}$ and $\nu_{(C=C)}$ modes showed bathochromic shift due to complexation. The $\nu_{(C=N)}$ peaks appeared at 1647, 1585, and 1630 cm^{-1} for **L**, **1**, and **2**, respectively. Moreover, the $\nu_{(C=C)}$ peaks were noted in the range of 1581–1480 cm^{-1}, 1534–1484 cm^{-1}, and 1538–1488 cm^{-1}, respectively. These spectral shifts provide strong evidence for the coordination of **L** with the two metal centers. Additionally, the peaks noted at 1383 and 1043 cm^{-1} in **2**, correspond to the asymmetric and symmetric vibrations of $\nu_{(N-O)}$, respectively [58–60].

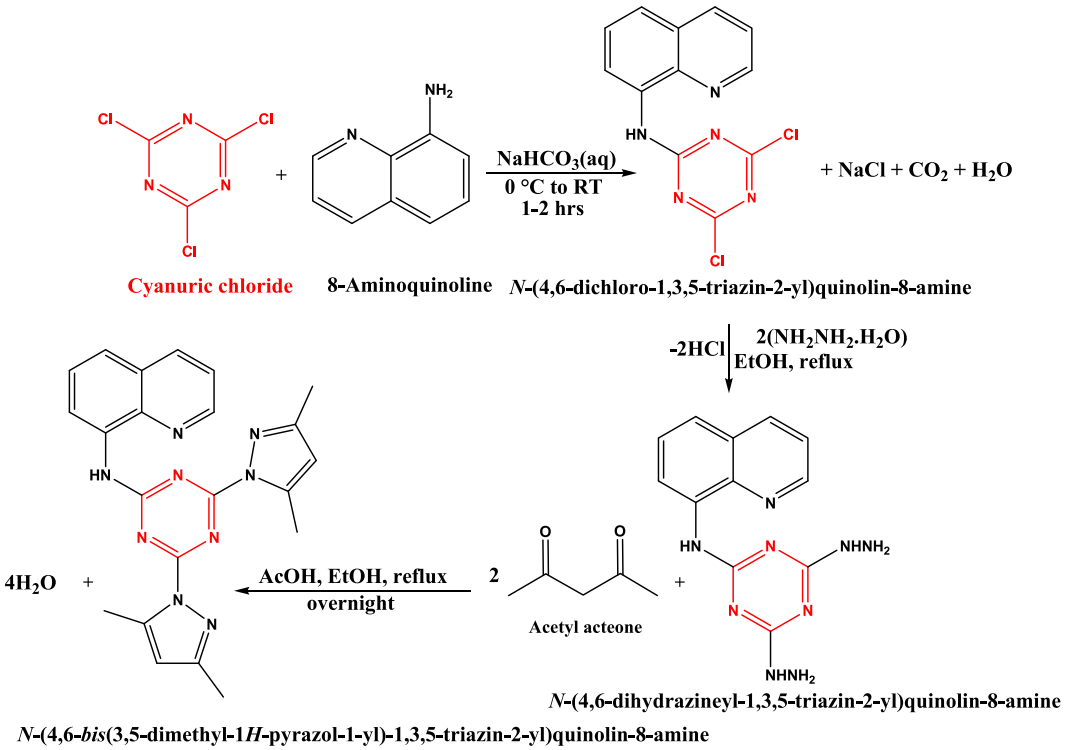

Scheme 1. Synthetic route of **L**.

The UV–Vis spectral analysis of the free ligand **L** and its complexes was conducted in DMSO (**Figs. S7-S8**). The spectrum of **L** displayed an absorption band at 330 nm, ascribed to the n → π* electronic transition [61,62]. Upon coordination with Mn(II) and Fe(III) ions, this band underwent a slight bathochromic shift to 335 nm, indicating a change in the electronic environment of the ligand due to metal coordination. Furthermore, the spectrum of **1** displayed a new broad band at 510 nm, which is characteristic of a d-d transition. This low-energy band appears with weak intensity, consistent with the spin- and Laporte-forbidden nature of d-d transitions in Mn(II) complexes [63]. Additionally, the spectrum of **2** revealed a new broad band at 645 nm, characteristic of ligand-to-metal charge transfer (LMCT) transitions, particularly from the bridging oxo ligand to the Fe(III) center [64–66]. This behavior is consistent with the previously reported ferric complexes exhibiting similar oxo-to-Fe(III) charge-transfer characteristics [67,68].

3.2. X-ray structure description

The structure of **1** was verified by single crystal X-ray diffraction analysis, indicating a mononuclear formula of [$MnLCl_2$] (Fig. 1). The crystal data parameters are listed in **Table S1**.

The crystal structure of **1** exhibited a single [$MnLCl_2$] molecule within the asymmetric formula. X-ray crystallographic analysis demonstrated that the Mn center is penta-coordinated with the ligand (**L**) in a pincer-like fashion, as shown in Fig. 1. The ligand (**L**) acts as a tridentate *NNN*-chelate, coordinated through three nitrogen atoms from pyrazole and *s*-triazine moieties. Notably, the Mn-$N_{(pyrazole)}$ bond lengths are slightly longer than the Mn-$N_{(s\text{-triazine})}$ bond. The Mn–N bond distances are 2.266(5) Å, 2.273(5) Å, and 2.211(4) Å for Mn01-N7, Mn01-N8, and Mn01-N4, respectively (Table 1). Moreover, the bite angles of **L** are 69.3(2)° and 70.0(2)° for N4-Mn01-N7 and N4-Mn01-N8, respectively. The coordination sphere is further completed by two chloride ions, where the Mn01–Cl and Mn01-Cl1 distances are 2.396(3) Å and 2.348(6) Å, respectively. The τ_5 parameter was calculated as 0.05 and 0.06 (for the disordered chloride ions), confirming a distorted square pyramidal geometry [69], as the maximum angle is 142.0(2)°. Furthermore, the Mn(II) atom deviates by 0.662 Å from the square plane, reduced to 0.575 Å in the case of the disordered chloride ions. In contrast, the previously reported [$Mn(^{Morph}BPT)_2$]$(ClO_4)_2$ (**3**), and [$Mn(^{Morph}BPT)(H_2O)_2NO_3$]$NO_3$ (**4**), based on the *NNN*-tridentate 4-(4,6-*bis*(3,5-dimethyl-1*H*-pyrazol-1-yl)-1,3,5-triazin-2-yl)morpholine (**^{Morph}BPT**) pincer ligand, exihibt a hexacoordinated, distorted octahedral geometry. The **^{Morph}BPT** ligand coordinates through its *NNN*-donor set with bite angels ranging from 69.49 to 71.14° and the Mn-$N_{(s\text{-triazine})}$ bonds are shorter than the Mn-$N_{(pyrazole)}$ bonds. The contrast between the pentacoordinated, square-pyramidal geometry of **1** and the hexacoordinated octahedral geometries of **3** and **4** underscores the crucial influence of ligand design, donor set, and overall structural assembly on the coordination environment of Mn(II) complexes with the *s*-triazine pincer ligands [70,71].

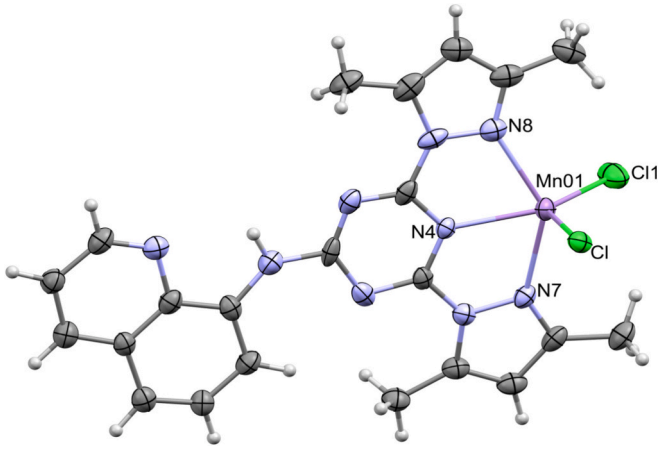

Fig. 1. ORTEP X-ray structure of **1** with thermal ellipsoids at 30% probability level. The disorder of the chloride ions was omitted for better clarity and is shown with details in **Fig. S9**.

Table 1
Bond lengths (Å) and angles (°) for **1.**

Bond	Distance	Bond	Distance
Mn01-N4	2.211(4)	Mn01-Cl1	2.348(6)
Mn01-N7	2.266(5)	Mn01-ClA	2.282(6)
Mn01-N8	2.273(5)	Mn01-Cl1A	2.270(8)
Mn01-Cl	2.396(3)		
Bond	**Angle**	**Bond**	**Angle**
N4-Mn01-N7	69.3(2)	N7-Mn01-Cl1	97.9(2)
N4-Mn01-N8	70.0(2)	N7-Mn01-ClA	106.2(4)
N7-Mn01-N8	138.5(2)	N7-Mn01-Cl1A	106.3(4)
N4-Mn01-Cl	101.4(2)	N8-Mn01-Cl	97.7(2)
N4-Mn01-Cl1	135.6(2)	N8-Mn01-Cl1	105.4(2)
N4-Mn01-ClA	118.7(6)	N8-Mn01-ClA	100.1(2)
N4-Mn01-Cl1A	142.0(2)	N8-Mn01- Cl1A	100.6(4)
N7-Mn01-Cl	97.9(1)	Cl-Mn01-Cl1	122.7(2)
Cl-Mn01-ClA	17.6(4)	Cl-Mn01-Cl1A	116.5(3)
Cl1-Mn01-ClA	105.7(4)	Cl1-Mn01-Cl1A	9.3(3)
ClA-Mn01-Cl1A	99.0(4)		

The non-classical C-H···Cl interactions primarily govern the packing of **1**. Various intermolecular C-H···Cl interactions are identified, with H···Cl distances ranging from 2.63 to 2.79 Å for the C15-H15···ClA and C2-H2A···Cl1 contacts, respectively (**Table S2**). In addition, two intramolecular interactions, C17-H17A···Cl1 and C18-H18A···Cl1A, are observed, with hydrogen-to-acceptor distances of 2.82 and 2.79 Å, respectively. A single classical intramolecular N2-H2···N1 hydrogen bond is also noted, with an H···N distance of 2.18 Å. Furthermore, two non-classical intramolecular C-H···N interactions are present, with H···N distances of 2.39 and 2.62 Å, for the C7-H7···N5 and C22-H22A···N3 interactions, respectively. The packing of **1** could therefore be described as a network extending along the *b*-axis (**Fig. S10**).

Comparable to hydrogen bonding, aromatic-aromatic and anion-π interactions play a vital role in molecular packing. Several π-π stacking interactions are noted between carbon atoms of the *s*-triazine and quinoline rings, with distances ranging from 3.251(9) to 3.524(8) Å for C8···C10 and C4···C11 contacts, respectively, as shown in Fig. 2 left. Additionally, a number of C···N contacts are observed, with distances ranging from 3.275(8) to 3.421(8) Å for C12···N1 and C5···N4 interactions, respectively (**Table S3**). Furthermore, three anion-π interactions between carbon atoms and chloride ions are revealed, with Cl···C distances of 3.231(1) Å, 3.335(9) Å, and 3.571(9) Å for Cl1···C2, Cl1···C3, and Cl···C20 contacts, respectively, as depicted in Fig. 2 right, and detailed in **Table S3**. The corresponding Cl-centroid distances are 4.193(10) Å for the first two contacts and 4.704(9) Å for the latter.

X-ray structure of **2** is depicted in Fig. 3, which reveals that compound **2** is a dinuclear complex comprising two crystallographically independent [$Fe_2L_2(\mu\text{-}O)(H_2O)_4$]$(NO_3)_4{\cdot}3H_2O$ units per asymmetric formula, with minor deviations observed in their geometric parameters, see **Fig. S11** bottom.

In the cationic inner sphere [$Fe_2L_2(\mu\text{-}O)(H_2O)_4$]$^{4+}$, each Fe center is hexacoordinated by three nitrogen atoms from **L** acting as an *NNN*-pincer chelator and two O-atoms from water molecules. The coordination environment is completed by bridging oxygen (μ-O) linking the two Fe centers. The bridged Fe–O bonds distances range from 1.773(4) to 1.792(4) Å, which are generally shorter than the Fe-OH_2 distances (1.971(5) to 2.137(5) Å) (Table 2). Additionally, the Fe-$N_{(pyrazole)}$ distances range from 2.157(6) to 2.195(6) Å, while the Fe-$N_{(s\text{-triazine})}$ distances range from 2.080(6) to 2.097(6) Å. Hence, Fe-$N_{(pyrazole)}$ bond distances are slightly longer than the Fe–N $_{(s\text{-triazine})}$, similar to **1**. These distances are indicative of a Fe(III) high spin configuration, as discussed in the introduction. The bite angles of **L** are in the range of 71.8(2)-73.0

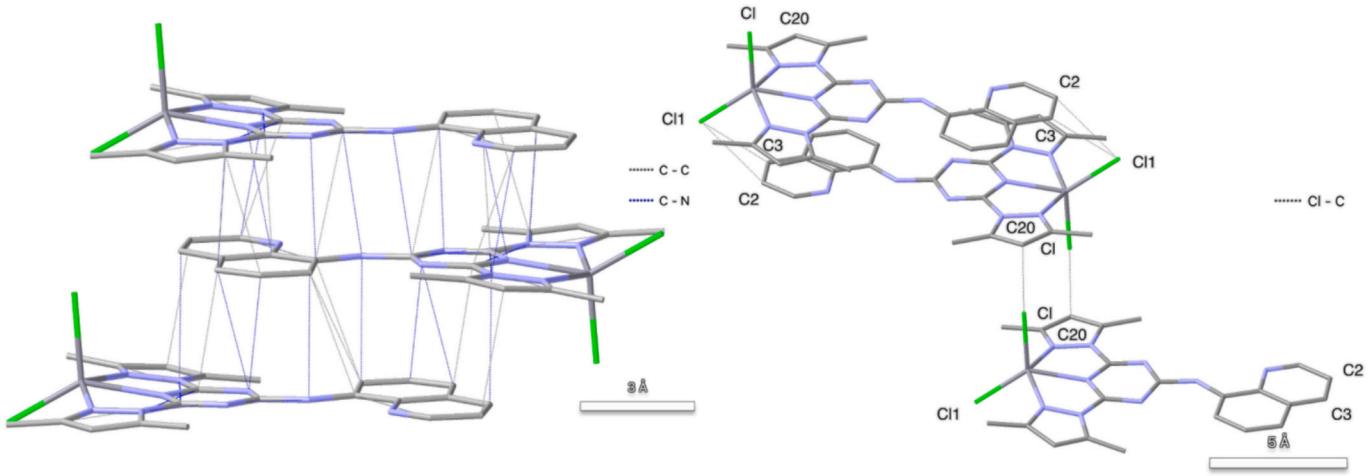

Fig. 2. π–π stacking (left, distance between 3.2 and 3.4 Å shown as dotted lines) and anion–π stacking, (right, distance between 3.2 and 3.6 Å shown as dotted lines) contacts for **1**. The hydrogen atoms were omitted for better clarity.

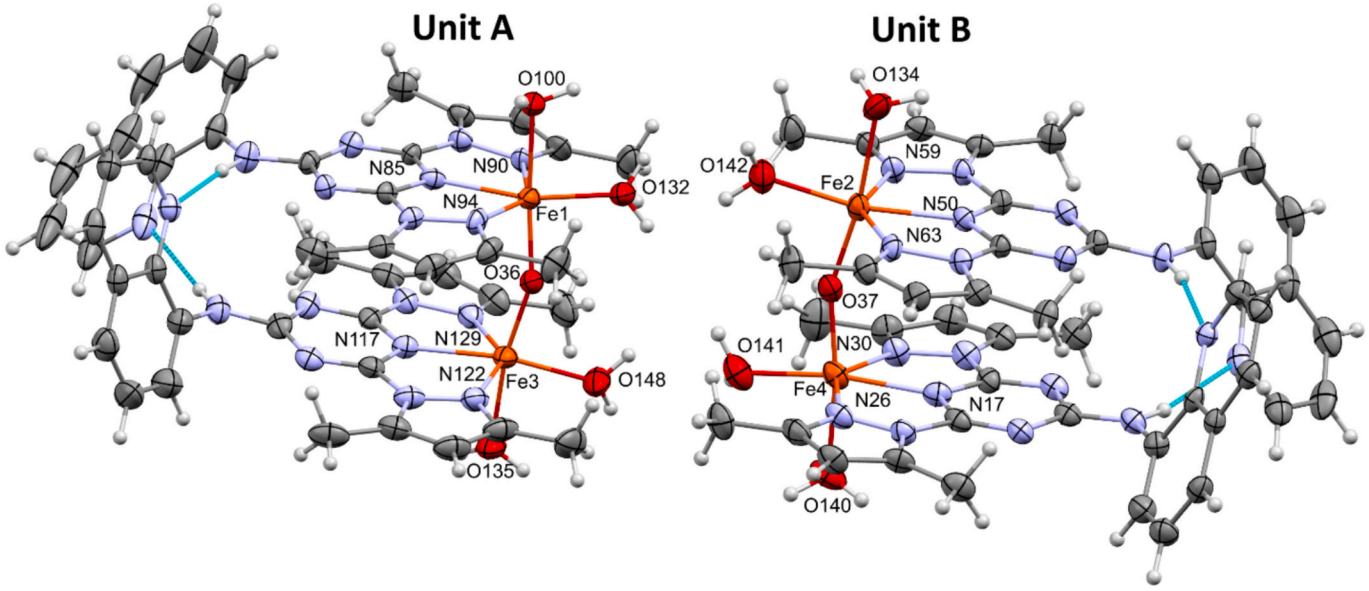

Fig. 3. ORTEP X-ray structure of **2**, showing intramolecular hydrogen bonding interactions. The nitrate groups and water molecules were omitted for better clarity and are shown with details in **Fig. S11** Top. The ellipsoids were drawn at the 30% probability level.

(2)°. In unit **A**, the trans O36-Fe1-O100 and O36-Fe3-O135 bond angles are 171.5(2) and 169.3(2)°, respectively. For unit **B**, the corresponding angles are 172.2(2) and 171.9(2)° for O37-Fe2-O134 and O37-Fe4-O140, respectively. Furthermore, the octahedral coordination environment around the Fe(III) centers was quantitatively assessed using the OctaDist 3.1.0 program [72]. Distortion parameters, including <D>, ζ, Δ, Σ, and Θ, were calculated for each crystallographically independent Fe center. The results indicated significant deviation from ideal octahedral geometry, likely due to ligand strain and packing effects, with Θ values of 358.764°, 389.371°, 369.494°, and 376.718° for Fe1, Fe2, Fe3, and Fe4, respectively (**Table S4**). The outer sphere of **2** contains four/nitrate groups along with three water molecules. It is worth to note that, the previously reported $[Fe_2(PMT)_2(H_2O)_4O](NO_3)_2$ (**5**), of 4,6-*bis*(3,5-dimethyl-1*H*-pyrazol-1-yl)-1,3,5-triazin-2(1*H*)-one (**HPMT**), was formed *via O*-demethylation of 2,4-*bis*(3,5-dimethyl-1*H*-pyrazol-1-yl)-6-methoxy-1,3,5-triazine ligand (**MBPT**) in the presence of $Fe(NO_3)_3$ generating the hydroxy-*s*-triazine derivative (**HPMT**). The hydroxy derivative then underwent keto-enol tautomerization followed by deprotonation to yield the $\mathbf{PMT}^-$ ligand, which acts as an anionic *NNN*-tridentate chelator, facilitating the assembly of *μ*-oxo-bridged dinuclear complex. Similar to **2**, **5** adopts a hexacoordinated dinuclear octahedral environment [73].

The supramolecular structure of **2** is controlled by two types of hydrogen-bonding interactions, O-H···O and N-H···N, as observed in **Fig. S12**. The intermolecular O-H···O hydrogen bonds are established, with the donor atoms being the oxygen atoms of water molecules, either coordinated to the metal center or present as lattice water molecules. Some of interactions feature hydrogen-to-acceptor distances ranging from 1.73 Å (O135-H13C···O174) to 2.58 Å (O133-H13N···O160) are listed in **Table S5** because the structure contains several donors and acceptors. In addition, four significant intramolecular N-H···N hydrogen bonds are identified, with hydrogen-to-acceptor distances ranging from 1.95 to 2.08 Å for N79-H79···N110 and N15-H15···N38 contacts, respectively. Moreover, the presence of water molecules as a solvent maximized the hydrogen bonding interactions.

In addition, the molecular packing of **2** showed a number of anion-π interactions occurred between the carbon and nitrogen atoms of the aromatic π-systems and the O-atoms of the nitrate groups, as shown in

Table 2
Bond lengths (Å) and angles (°) for **2**.

Bond	Length	Bond	Length
Fe1-N85	2.080(6)	Fe3-N117	2.097(6)
Fe1-N90	2.194(6)	Fe3-N122	2.184(7)
Fe1-N94	2.176(6)	Fe3-N129	2.167(7)
Fe1-O36	1.779(4)	Fe3-O36	1.773(4)
Fe1-O100	2.095(4)	Fe3-O135	2.083(5)
Fe1-O132	1.971(5)	Fe3-O148	1.981(6)
Fe2-N50	2.081(5)	Fe4-N17	2.082(6)
Fe2-N59	2.195(5)	Fe4-N26	2.182(6)
Fe2-N63	2.195(6)	Fe4-N30	2.157(6)
Fe2-O37	1.792(4)	Fe4-O37	1.780(5)
Fe2-O134	2.137(5)	Fe4-O140	2.081(5)
Fe2-O142	1.993(5)	Fe4-O141	1.991(6)
Bond	**Angle**	**Bond**	**Angle**
N85-Fe1-N90	72.7(2)	N117-Fe3-N122	72.0(2)
N85-Fe1-N94	73.0(2)	N117-Fe3-N129	72.0(2)
N94-Fe1-N90	145.6(2)	N129-Fe3-N122	143.7(2)
O36-Fe1-N85	100.2(2)	O36-Fe3-N117	101.3(2)
O36-Fe1-N90	98.9(2)	O36-Fe3-N122	98.2(2)
O36-Fe1-N94	88.9(2)	O36-Fe3-N129	93.1(2)
O100- Fe1- N85	85.1(2)	O135-Fe3-N117	88.9(2)
O100-Fe1-N90	89.1(2)	O135-Fe3-N122	88.2(2)
O100-Fe1-N94	86.2(2)	O135-Fe3-N129	86.7(2)
O132-Fe1-N85	166.4(2)	O148-Fe3-N117	170.5(2)
O132-Fe1-N90	101.7(2)	O148-Fe3-N122	104.6(3)
O132-Fe1-N94	111.3(2)	O148-Fe3-N129	110.2(3)
O36-Fe1-O100	171.5(2)	O36-Fe3-O135	169.3(2)
O36-Fe1-O132	92.9(2)	O36-Fe3-O148	87.9(2)
O132-Fe1-O100	82.4(2)	O148-Fe3-O135	82.1(2)
N50-Fe2-N59	72.6(2)	N17-Fe4-N26	71.8(2)
N50-Fe2-N63	72.3(2)	N17-Fe4-N30	72.7(2)
N63-Fe2-N59	144.9(2)	N30-Fe4-N26	144.4(2)
O37-Fe2-N50	101.1(2)	O37-Fe4-N17	99.4(2)
O37-Fe2-N59	94.8(2)	O37-Fe4-N26	94.6(2)
O37-Fe2-N63	94.1(2)	O37-Fe4-N30	93.6(2)
O134-Fe2-N50	86.7(2)	O140-Fe4-N17	88.6(2)
O134-Fe2-N59	87.4(2)	O140-Fe4-N26	88.7(2)
O134-Fe2-N63	88.4(2)	O140-Fe4-N30	87.9(2)
O142-Fe2-N50	168.0(2)	O141-Fe4-N17	170.8(2)
O142-Fe2-N59	107.1(2)	O141-Fe4-N26	107.5(2)
O142-Fe2-N63	106.7(2)	O141-Fe4-N30	107.1(2)
O37-Fe2-O134	172.2(2)	O37-Fe4-O140	171.9(2)
O37-Fe2-O142	90.9(2)	O37-Fe4-O141	89.9(2)
O142-Fe2-O134	81.3(2)	O141-Fe4-O140	82.1(2)

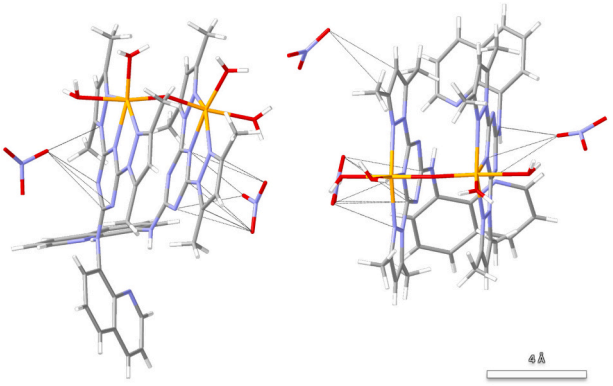

Fig. 4. Anion–π stacking contacts for **2.** O···N and O···C distances between 3.2 and 3.6 Å are shown as dotted lines.

Fig. 4. There are enormous numbers of π-π interactions in **2** due to the number of aromatic rings, with the shortest distance of 3.461(3) Å between two adjacent *s*-triazine rings. Other interactions that also stabilize the crystal structure, such as Fe···π, X-H···π and N–O···π, are also found. The shortest observed C···O interaction is (C49···O172) with a distance of 2.752(1) Å, and an O-centroid distance of 2.852(11) Å. While the longest one is 3.248(8) Å for C20···O139, with an O-centroid distance of 2.935(10) Å. Moreover, N···O interactions are observed, with distances ranging from 2.835(1) to 3.154(2) Å for the N50···O172 and N113···O176 interactions, and corresponding O-centroids distances of 2.852(11) and 2.882(9) Å, respectively (**Table S6**).

3.3. Molecular packing Hirshfeld analysis

Hirshfeld surface analysis constitutes a robust computational approach for quantitatively and qualitatively examining intermolecular interactions in crystalline solids [74]. It provides detailed insight into non-covalent interactions, such as π-π interactions and hydrogen bonding, which are critical in determining the supramolecular structure [75]. The Hirshfeld d_{norm} surfaces for both complexes are displayed in Fig. 5, without including nitrate anions and water molecules. For simplicity, **2** is represented by two units, **2(A)** and **2(B)**. In both complexes, π-π stacking interactions are evidenced by the presence of blue/red triangles on the shape index map, and flat green regions on the curvedness map (**Fig. S13**).

In **1**, the d_{norm} surface reveals key intermolecular interactions, such as Mn···C (0.6%), C···Cl (0.4%), H···Cl (20.7%), C···C (5.0%), and C···H (11.3%), as prominent red spots, highlighting their critical contribution to crystal packing (Fig. 6). The associated fingerprint plots exhibit sharp spikes corresponding to H···Cl interactions, underscoring their significance among the observed interactions. Additionally, the symmetrical appearance of the spikes related to Cl···H/H···Cl contacts suggests that the surface engages in Cl···H interactions as both a hydrogen bond donor and acceptor.

On the other hand, O···N, O···H, O···C, N···H, N···C, H···H, and H···C contacts are revealed to significantly influence the molecular packing of **2**, since they appear as red spots in their d_{norm} maps (Fig. 7), with percentage contributions of 1.4, 33.6, 1.7, 5.7, 0.3, 39.7, and 16.0% in unit **A**, and 1.4, 32.0, 2.2, 5.6, 0.3, 40.3, and 15.9% in unit **B**, respectively. Notably, O···H appears as a sharp spike in the fingerprint plot, highlighting its impact on the molecular packing. Furthermore, the asymmetry of the spikes related to O···H/H···O contacts indicates that the surface predominantly acts as a hydrogen bond donor in this case.

A detailed breakdown of all possible contacts within the crystal structure is provided in **Table S7**. In **1**, the dominant interactions are H···H (43.3%), Cl···H (20.7%), and C···H (11.3%) (Fig. 8). For **2**, unit **A** exhibits H···H, O···H, and H···C interactions contributing 39.7%, 33.6% and 16.0%, respectively. The corresponding values for unit **B** are 40.3%, 32.0%, and 15.9%, respectively.

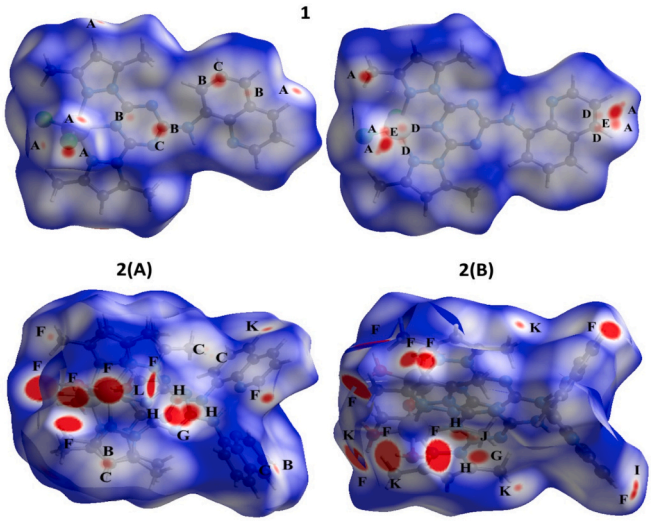

Fig. 5. Full d_{norm} maps for **1, 2(A),** and **2(B)**. The most predominant interactions are H···Cl (**A**), C···C (**B**), H···C (**C**), Mn···C (**D**), C···Cl (**E**), O···H (**F**), O···N (**G**), O···C (**H**), N···H (**I**), N···C (**J**), H···H (**K**), and O···O (**L**).

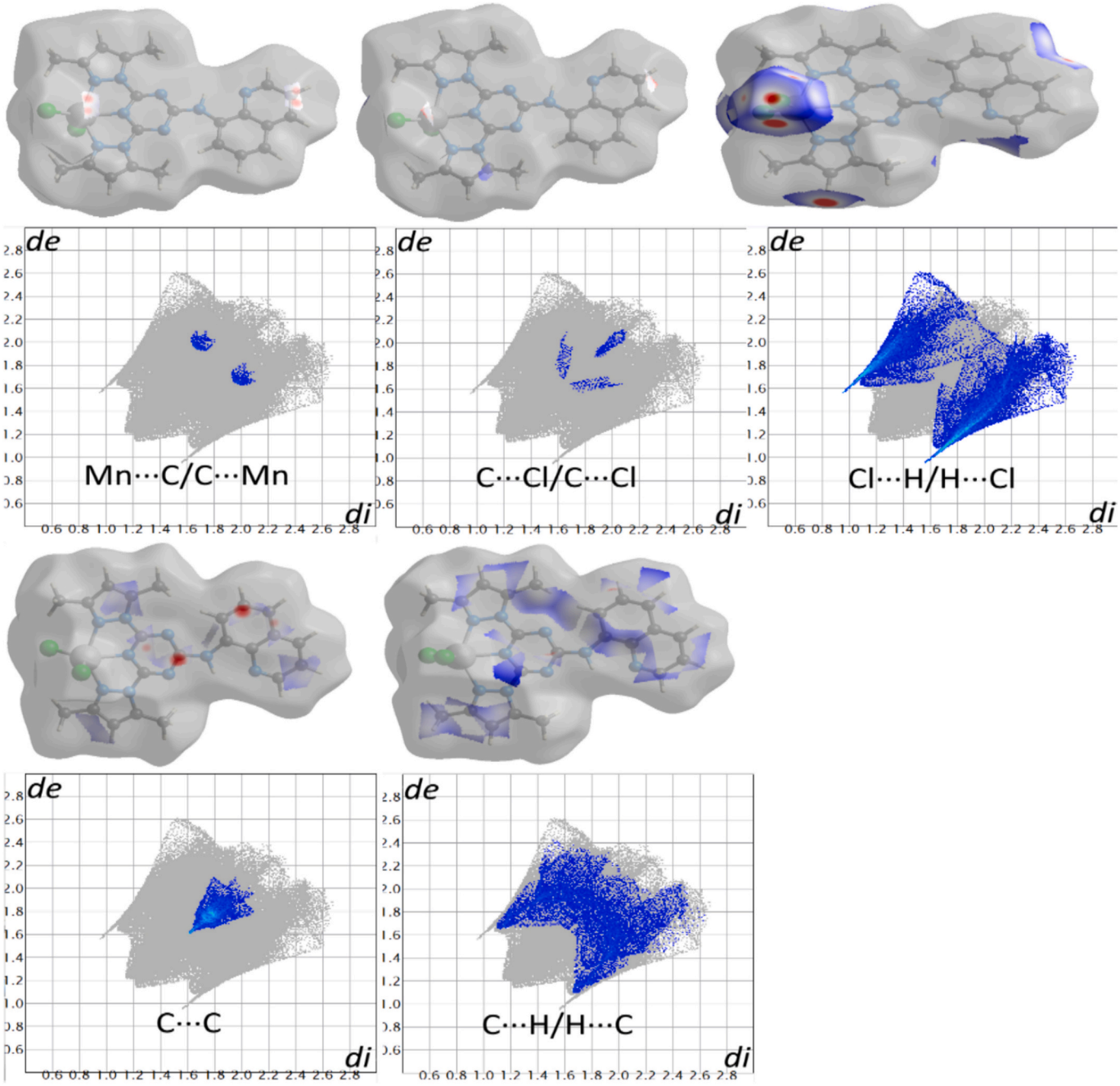

Fig. 6. The decomposed d_{norm} maps and fingerprint plots for significant contacts in **1**.

3.4. Enrichment ratio analysis

The tendency of atomic pairs within the crystal structure to engage in intermolecular interactions was assessed utilizing the methodology outlined by Jelsch et al. [76] The enrichment ratio can be quantified by taking the ratio of the observed percentage of C_{XX} or C_{XY} contacts in the crystal relative to the respective theoretical random contact ratios, R_{XX} and R_{XY}, respectively. For E_{XY} exceeding 1, generally signifies a favorable interaction between atom pairs and indicating a higher likelihood of contact formation within the crystal. In contrast, an E_{XY} value below 1 reflects a diminished interaction tendency, implying that the atom pairs are disfavored in terms of spatial association within the crystalline structure.

In **1,** the enrichment ratio is greater than one for Cl···H, N···C, C···C and H···H, (**Table S8**). For **2**, it is greater than one for O···N, O···H, N···H, H···C, and C···C, reflecting a strong inclination of these atom pairs to participate in intermolecular interactions within the crystal structure. Conversely, the enrichment ratio for Cl···N, Cl···C, N···N, N···H, and C···H interactions in **1** is below unity, indicating a reduced likelihood of these contacts occurring within the crystal. Similarly, enrichment ratios below one for O···O, O···C, and H···H interactions in **2**, indicate a diminished propensity for these interactions in the crystal. In **1**, E_{XY} of Cl···H and C···C contacts, and in **2**, the enrichment of O···H and N···H contacts, highlights the role of the hydrogen bonding and π···π stacking interactions in stabilizing their packing. In contrast, the lower values of E_{XY} for Cl···N and N···N contacts in **1**, and O···O contacts in **2**, indicated they are less favored interactions to be occurred. Overall, the enrichment ratio analysis quantitatively supports the Hirshfeld and fingerprint plot results, identifying the statistically preferred interactions in their solid state.

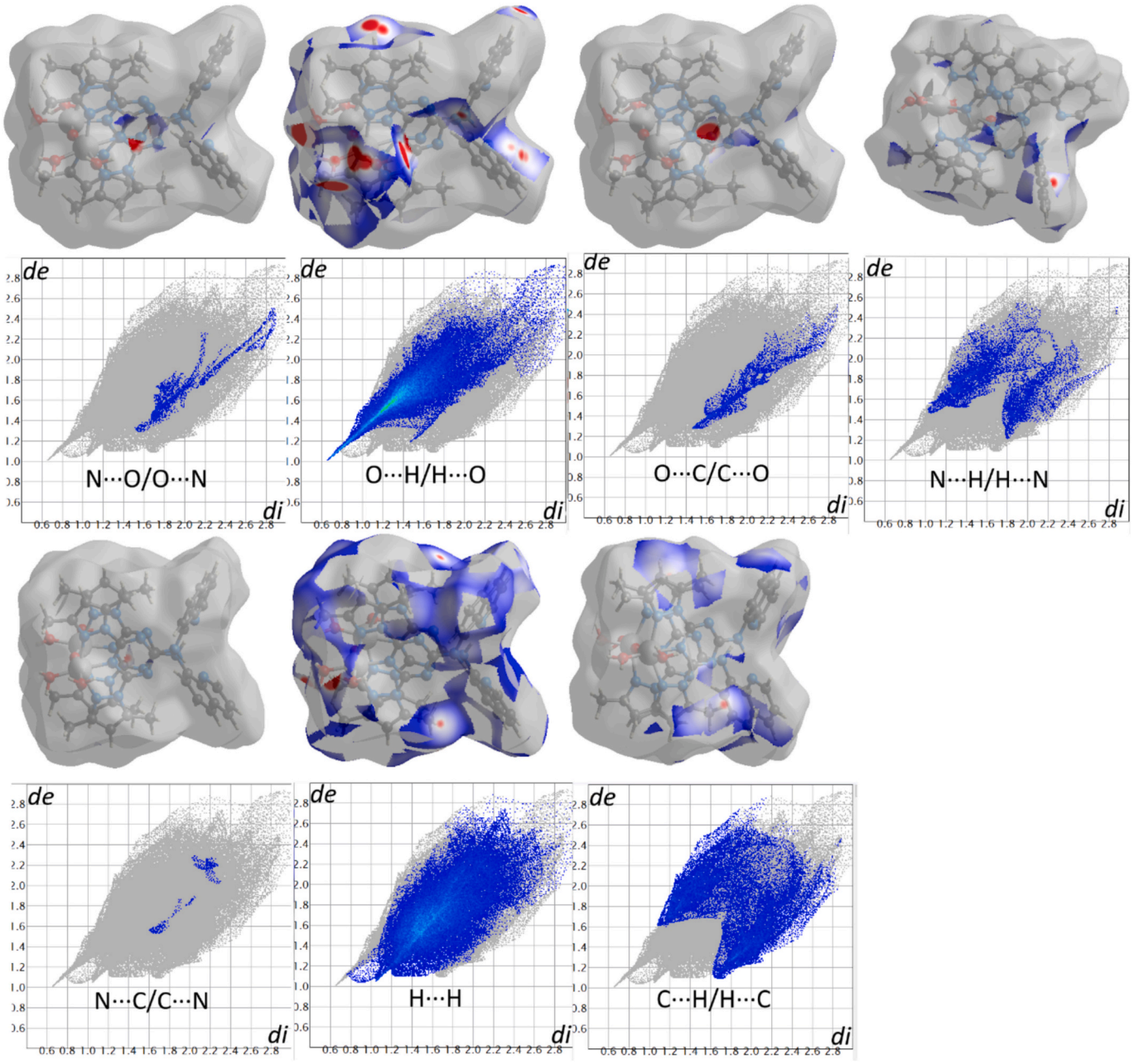

Fig. 7. The decomposed d_{norm} maps and fingerprint plots for significant contacts in **2**.

3.5. AIM topology analysis

To gain insight into the bonding characteristics of the investigated complexes, a topological analysis based on the quantum theory of atoms in molecules (AIM) was conducted for **1** and **2**, with Mn and Fe in the high-spin state due to the well-known weak ligand field imposed by nitrogen donors of *s*-triazine pincer ligands [77,78]. This analysis focused on identifying bond critical points (BCPs) and evaluating several key descriptors, including electron density (ρ), Lagrangian kinetic energy (G), Hamiltonian kinetic energy (K), potential energy density (V), total energy density (H), Laplacian of electron density ($\nabla^2\rho$), and the energy ratio ($|V(r)|/G(r)$), all of which together provide a detailed picture of the bond nature. The topological parameters are summarized in **Table S9**.

For **1**, the electron density values (ρ) are less than 0.1 a.u. and Laplacian values ($\nabla^2\rho$) are positive for all interactions. Hence, these interactions can be characterized as mostly closed-shell in nature [79]. Furthermore, analysis of the total energy density H(r) confirms that its positive or slightly negative value reflects predominantly closed-shell interactions [80]. Additionally, $|V(r)|/G(r)$ ratios exceeding 1 suggest that Mn–Cl bonds possess a modest degree of covalent character [81,82], whereas values below one for Mn–N confirm the presence of closed-shell interactions.

On the other hand, AIM analysis of **2** reveals ρ(r) values below 0.1 a.u for Fe–N and terminal Fe–O bonds, indicating a closed-shell nature for these bonding interactions. However, the bridged Fe–O bonds have ρ(r) exceeding 0.1 a.u., reflect enhanced electron localization due to shared interactions between the two Fe centers, which indicate a greater degree of covalency. Furthermore, analysis of the total energy density H(r) reveals positive or marginally negative values, which are indicative of a closed-shell interaction for most coordination bonds [80], except for Fe–O bonds involving the bridging oxygen, which show negative H(r) values, pointing to a modest covalent contribution [81,82]. Additionally, the $|V(r)|/G(r)$ ratios exceeding unity suggest a partial covalent

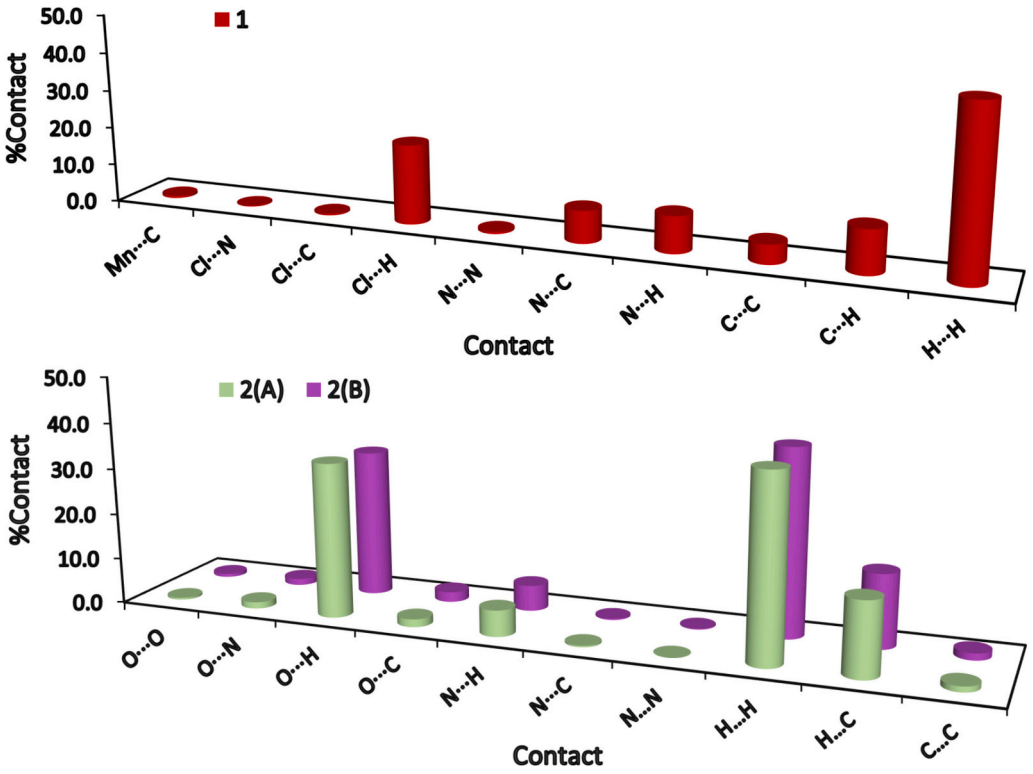

Fig. 8. All possible intermolecular contacts and their percentages in **1** and **2**.

character [80,83,84] while those less than 1 confirm closed-shell interactions [81,82]. Moreover, an inverse relationship is observed between the electron density and the corresponding Mn–N and Fe–N bond lengths, as illustrated in (Fig. 9). The correlation coefficients (R^2) are close to 1, confirming the reliability of the observed bonding trends.

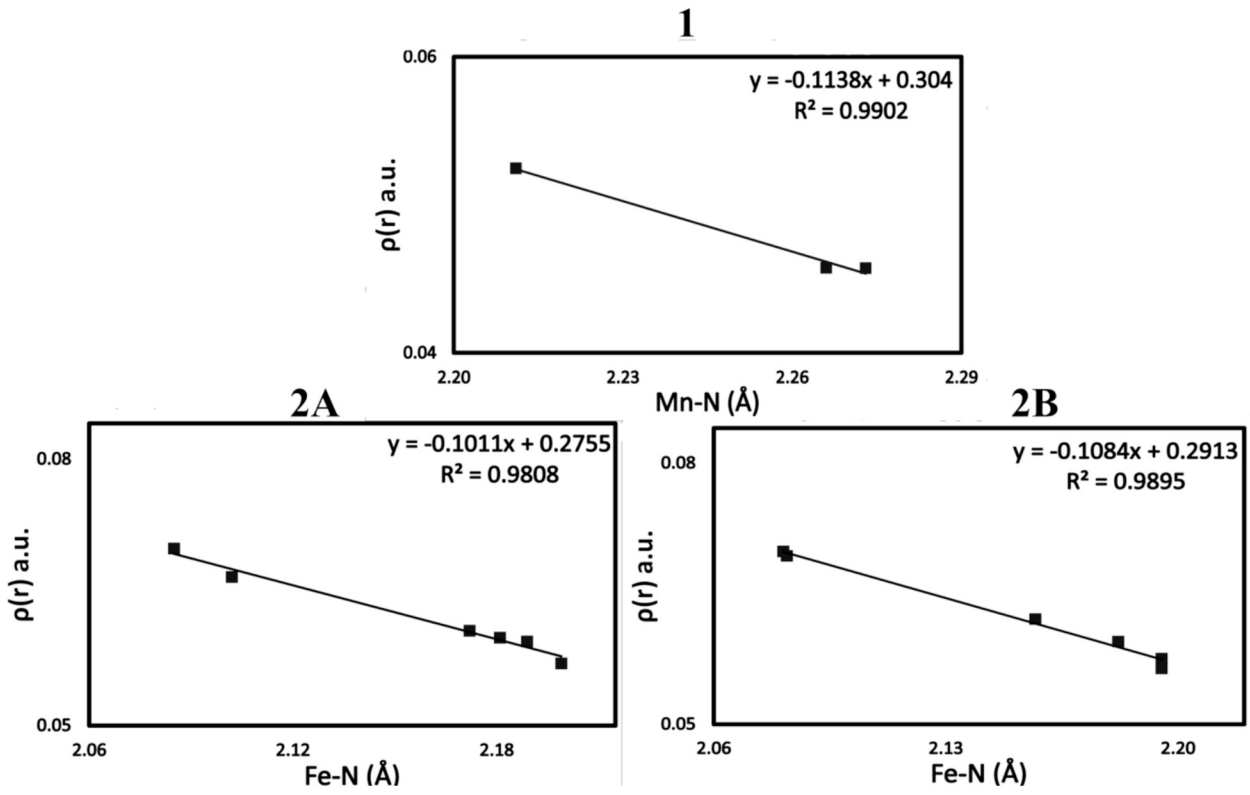

Fig. 9. Correlation between the ρ(r) with Mn–N (**1**), Fe–N (**2 A** and **2B**) bond distances.

3.6. Biological studies

3.6.1. Anticancer activity

Lung and colon cancer are among the leading causes of global cancer-related mortality, accounting for the highest fatality rates among human malignancies [85]. *In vitro* cytotoxicity of **L**, **1**, and **2** against the lung A-549 and colon HCT-116 carcinoma cell lines was assessed using the MTT assay (Tables 3 and **S10-S18**). Against HCT-116 colon carcinoma cell line, **1** and **2** exhibited significantly lower IC_{50} values (24.3 ± 0.39, and 9.05 ± 0.21 μM, respectively) than the free ligand **L** (133.25 ± 3.52 μM). A similar pattern was observed for the A-549 lung carcinoma cell line where **L**, **1**, and **2** gave IC_{50} values of 149.71 ± 4.06, 36.4 ± 0.70, and 10.67 ± 0.25 μM, respectively indicating that complexation significantly enhances anticancer activity. Notably, **2** demonstrated superior cytotoxicity over **1** towards both cell lines. To assess biocompatibility, the cytotoxicity of the compounds was also tested on normal WI-38 fibroblast cells. The selectivity index (SI) was calculated for each compound to determine its therapeutic window. The SI values for **L**, **1**, and **2** all exceeded unity, indicating their safety and promising potential as anticancer agents. Among the tested compounds, **1** and **2** exhibited markedly enhanced cytotoxic activity relative to *cis*-platin, particularly against the HCT-116 colon cancer cell line, being approximately 1.2- and 3.1-fold more potent, respectively. Also, **1** and **2** were compared to the structurally related analogues; **3** and **5**, (from references 70 and 73), against the A-549 lung carcinoma cell line. Complex **3** exhibited IC_{50} of 40.2 ± 2.70 μM, showing lower cytotoxic effects compared to **1** [70]. Also, **5** exhibited an IC_{50} value of 8.56 ± 0.42 μM, showing slightly higher cytotoxic effects compared to **2** [73].

3.6.2. Antimicrobial activity

The antimicrobial activity of the free ligand **L** and its corresponding pincer complexes; **1** and **2** was assessed against a panel of clinically relevant pathogenic microorganisms. The inhibition zone diameters (IZDs) and minimum inhibitory concentrations (MICs) are summarized in Table 4. The ligand and its complexes exhibited moderate antimicrobial activity, with IZDs generally larger against bacterial strains (12–18 mm) than fungal strains (9–11 mm). Moreover, the MIC values fall within the ranges of 156–1250 μg/mL for bacteria and 1250–2500 μg/mL for fungi. The free ligand **L** exhibited higher antibacterial activity against Gram-positive bacteria. In comparison, **1** showed slightly reduced activity, while **2** displayed comparatively lower efficacy against the same strains. Conversely, **2** showed enhanced antibacterial efficacy against Gram-negative bacteria compared to **1** and **L**. Moreover, no detectable activity was observed against *A. fumigatus* for all studied compounds. Notably, good antifungal activity was detected against *C. albicans*, with the free ligand being more active than **1** and **2**. These complexes exhibited moderate antibacterial activity compared to the control gentamycin. Also, their activities against *C. albicans* are weak compared to ketoconazole. Unlike the quinoline-containing ligand (**L**), which exhibited broad-spectrum antimicrobial activity (except *against A. fumigatus*), **^{Morph}BPT** showed no detectable activity. This suggests that the presence of the quinoline moiety is critical for bioactivity which agrees with its well-established biological significance as an antimicrobial agent [88]. Additionally, **1** demonstrated enhanced antibacterial efficacy against *E. coli* (IZD = 13 mm) compared to **3,** which showed no observable activity [70]. In contrast, **1** displayed lower effectiveness against *S. aureus*, *B. subtilis*, and *P. vulgaris* (IZDs = 15, 17 and 12 mm, respectively) compared to **3** (IZDs = 20, 21 and 29 mm, respectively). Moreover, **2** exhibited enhanced antimicrobial activity against *E. coli*, *P. vulgaris*, and *B. subtilis* compared to **5** (IZDs = 8, 14, and 14 mm, respectively) [73]. In contrast, the latter demonstrated higher efficacy against *S. aureus, C. albicans*, and *A. fumigatus*, with IZD values of 15, 10, and 12 mm, respectively.

Table 3
Cytotoxicity of **1**, **2**, and **L** against HCT-116, A-549, and WI-38 cells and their selectivity indices (SI) utilizing MTT assay.

Compound	HCT-116	SI	A-549	SI	WI-38
L	133.25 ± 3.52	2.04	149.71 ± 4.06	1.81	271.59 ± 5.18
1	24.32 ± 0.39	2.32	36.48 ± 0.71	1.54	56.32 ± 1.53
2	9.06 ± 0.21	2.01	10.68 ± 0.26	1.70	18.19 ± 0.46
3[a]	–	–	40.2 ± 2.7	2.8	111.6 ± 3.8
5[b]	–	–	8.56 ± 0.42	–	–
cis-Platin	27.99 ± 2.66[c]	11.09	6.0.39 ± 0.73[d]	48.58	310.4 ± 10.33

[a] ref. 70 [b] ref. 73, [c] ref. 86, [d] ref. 87.

Table 4
Inhibition zone diameters (IZDs; mm) and minimum inhibitory concentrations (MIC; μg/mL) of **L**, **1**, and **2** against selected microbial strains.

Microorganism	L	1	2	3	5	Control
S. aureus	15(312)	15(625)	13 (625)	20	15	24(9.7)[b]
B. subtilis	18(156)	17(312)	16 (312)	21	14	26(4.8)[b]
E. coli	14(625)	13(625)	14 (625)	NA[a]	8	30(4.8)[b]
P. vulgaris	14(625)	12 (1250)	15 (625)	29	14	25(4.8)[b]
A. fumigatus	NA[a]	NA[a]	NA[a]	17	12	17 (156)[c]
C. albicans	11 (1250)	10 (2500)	9 (2500)	18	10	20 (312)[c]

[a] NA: No activity, [b] Gentamycin, [c] Ketoconazole.

4. Conclusions

This study presents the synthesis, characterization, and biological evaluation of two d^5 metal complexes [$MnLCl_2$]; **1** and [$Fe_2L_2(\mu$-O)$(H_2O)_4](NO_3)_4{\cdot}3H_2O$; **2**, based on a novel *s*-triazine pincer-type ligand (**L**). The complexes were synthesized *via* a self-assembly approach by mixing an ethanolic solution of **L** with either $MnCl_2.4H_2O$ or $Fe(NO_3)_3.9H_2O$ in ethanol. **1** is mononuclear with penta-coordinated Mn (II) ion with a square-pyramidal geometry, while **2** is dinuclear comprising μ-oxo bridge between the two metal centers, which are hexacoordinated and exhibit a distorted octahedral geometry. Moreover, Hirshfeld analysis and enrichment ratio calculations were performed to investigate the significant interactions within the crystals. AIM analysis revealed that the Mn–N, Fe–N, and terminal Fe–O bonds exhibit predominantly closed-shell characteristics, whereas the Mn–Cl and bridging Fe–O bonds demonstrate partial covalent character. The free ligand and its complexes were evaluated for their anticancer and antimicrobial activities. Biological evaluation revealed that both complexes **1** and **2** exhibited enhanced cytotoxicity compared to **L**, with complex **2** displaying markedly superior cytotoxicity relative to complex **1** across both cancer cell lines, implying a considerable enhancement in anticancer efficacy upon complexation. Furthermore, the free ligand **L** exhibited good antimicrobial activity against Gram-positive bacteria, while **2** exhibited better antimicrobial against Gram-negative bacteria.

Declaration of competing interest

The authors declare that they have no known competing financial interests or personal relationships that could have appeared to influence the work reported in this paper.

Acknowledgments

This work was carried out in part at the Chalmers Material Analysis

Laboratory, CMAL. Funding for this work was provided by Chalmers University of Technology through the GENIE project, and we also thank the Swedish Research Council (Grant No. 2020-04029) and the Olle Engkvist Foundation for funding the single crystal diffractometer.

Appendix A. Supplementary data

Supplementary data to this article can be found online at https://doi.org/10.1016/j.ica.2026.123114.

Data availability

All the data utilized in this study are included in the manuscript and its supplementary materials.

References

[1] C.G. Retnam, S.V. Rose, B.S. Kumari, Synthesis, characterization, biological activity and molecular docking study of transition metal complexes from heterocyclic ligand system, J. Mol. Struct. 1282 (2023) 135162.
[2] H. Liao, M. Liu, M. Wang, D. Zhang, Y. Hao, F. Xie, Exploring the potential of *s*-Triazine derivatives as novel antifungal agents: a review, Pharmaceuticals 18 (2025) 690.
[3] B. Kolesinska, K. Barszcz, Z.J. Kaminski, D. Drozdowska, J. Wietrzyk, M. Switalska, Synthesis and cytotoxicity studies of bifunctional hybrids of nitrogen mustards with potential enzymes inhibitors based on melamine framework, J. Enzyme Inhib. Med. Chem. 27 (2012) 619–627.
[4] J. Chu, W. Chen, G. Su, Y.-F. Song, Four new copper(II) complexes with di-substituted *s*-triazine-based ligands, Inorg. Chim. Acta 376 (2011) 350–357.
[5] T.J. Mooibroek, P. Gamez, The *s*-triazine ring, a remarkable unit to generate supramolecular interactions, Inorg. Chim. Acta 360 (2007) 381–404.
[6] F. Ugozzoli, C. Massera, Intermolecular interactions between benzene and 1,3,5-triazine: a new tool for crystal engineering and molecular recognition, CrystEngComm 7 (2005) 121–128.
[7] G. Blotny, Recent applications of 2, 4, 6-trichloro-1,3,5-triazine and its derivatives in organic synthesis, Tetrahedron 62 (2006) 9507–9522.
[8] C.P. Wild, E. Weiderpass, B.W. Stewart, World cancer Report, 2020.
[9] D.R. Shah, R.P. Modh, K.H. Chikhalia, Privileged *s*-triazines: structure and pharmacological applications, Future Med. Chem. 6 (2014) 463–477.
[10] P. Singla, V. Luxami, K. Paul, Triazine as a promising scaffold for its versatile biological behavior, Eur. J. Med. Chem. 102 (2015) 39–57.
[11] T. Kubo, C.A. Figg, J.L. Swartz, W.L. Brooks, B.S. Sumerlin, Multifunctional homopolymers: postpolymerization modification *via* sequential nucleophilic aromatic substitution, Macromolecules 49 (2016) 2077–2084.
[12] Adams, M.; McVey, M.; Sekelsky, J.; Andrulis, E.; Werner, J.; Nazarian, A.; ErdjumentBromage, H.; Auluck, P.; Chan, H.; Trojanowski, J. Degenerative diseases. *Genome* 2002, 420, 666–669.
[13] A. Bazgir, M.M. Khanaposhtani, A.A. Soorki, One-pot synthesis and antibacterial activities of pyrazolo [4′, 3′: 5, 6] pyrido [2, 3-d] pyrimidine-dione derivatives, Bioorg. Med. Chem. Lett. 18 (2008) 5800–5803.
[14] A.M. Gilbert, A. Failli, J. Shumsky, Y. Yang, A. Severin, G. Singh, W. Hu, D. Keeney, P.J. Petersen, A.H. Katz, Pyrazolidine-3, 5-diones and 5-hydroxy-1 H-pyrazol-3 (2*H*)-ones, inhibitors of UDP-N-acetylenolpyruvyl glucosamine reductase, J. Med. Chem. 49 (2006) 6027–6036.
[15] X.-H. Liu, P. Cui, B.-A. Song, P.S. Bhadury, H.-L. Zhu, S.-F. Wang, Synthesis, structure and antibacterial activity of novel 1-(5-substituted-3-substituted-4, 5-dihydropyrazol-1-yl) ethanone oxime ester derivatives, Bioorg. Med. Chem. 16 (2008) 4075–4082.
[16] O. Prakash, R. Kumar, V. Parkash, Synthesis and antifungal activity of some new 3-hydroxy-2-(1-phenyl-3-aryl-4-pyrazolyl) chromones, Eur. J. Med. Chem. 43 (2008) 435–440.
[17] A. Tiwari, A. Mishra, S. Mishra, B. Mamba, B. Maji, S. Bhattacharya, Synthesis and DNA binding studies of Ni (II), co (II), cu (II) and Zn (II) metal complexes of N1, N5-bis [pyridine-2-methylene]-thiocarbohydrazone Schiff-base ligand, Spectrochim. Acta A 79 (2011) 1050–1056.
[18] P. Teng, C. Li, Z. Peng, V.A. Marie, A. Nimmagadda, M. Su, Y. Li, X. Sun, J. Cai, Facilely accessible quinoline derivatives as potent antibacterial agents, Bioorg. Med. Chem. 26 (2018) 3573–3579.
[19] B. Abdi, M. Fekadu, D. Zeleke, R. Eswaramoorthy, Y. Melaku, Synthesis and evaluation of the antibacterial and antioxidant activities of some novel chloroquinoline analogs, J. Chem. 2021 (2021) 2408006.
[20] S. Kumar Gupta, A. Mishra, Synthesis, characterization & screening for anti-inflammatory & analgesic activity of quinoline derivatives bearing azetidinones scaffolds, Antiinflamm. Antiallergy Agents Med. Chem. 15 (2016) 31–43.
[21] F.E. Goda, A.-M. Alaa, H.A. Ghoneim, Synthesis and biological evaluation of novel 6-nitro-5-substituted aminoquinolines as local anesthetic and anti-arrhythmic agents: molecular modeling study, Bioorg. Med. Chem. 13 (2005) 3175–3183.
[22] R.K. Sodhi, S. Paul, Metal complexes in medicine an overview and update from drug design perspective, CTOIJ 14 (2019) 25–32.
[23] M. Williams, G. Todd, N. Roney, J. Crawford, P. Coles McClure, J. Garey, K. Zaccaria, M. Citra, Toxicological Profile for Manganese. US Department of Health and Human Services. Public Health Service, 2012.
[24] Intakes, S.C.o.t.S.E.o.D.R.; Interpretation, S.o.; Intakes, U.o.D.R.; Nutrients, S.o.U. R.L.o.; Micronutrients, P.o, Dietary reference intakes for vitamin A, vitamin K, arsenic, boron, chromium, copper, iodine, iron, manganese, molybdenum, nickel, silicon, vanadium, and zinc, National Academies Press, 2002.
[25] L. Li, X. Yang, The essential element manganese, oxidative stress, and metabolic diseases: links and interactions, Oxid. Med. Cell. Longev. 2018 (2018) 7580707.
[26] K. Barnese, E.B. Gralla, J.S. Valentine, D.E. Cabelli, Biologically relevant mechanism for catalytic superoxide removal by simple manganese compounds, Proc. Natl. Acad. Sci. U. S. A. 109 (2012) 6892–6897.
[27] D. Salvemini, D.P. Riley, S. Cuzzocrea, SOD mimetics are coming of age, Nat. Rev. Drug Discov. 1 (2002) 367–374.
[28] B. Drahoš, I. Lukeš, É. Tóth, Manganese (II) complexes as potential contrast agents for MRI, Eur. J. Inorg. Chem. 2012 (2012) 1975–1986.
[29] A. Gupta, P. Caravan, W.S. Price, C. Platas-Iglesias, E.M. Gale, Applications for transition-metal chemistry in contrast-enhanced magnetic resonance imaging, Inorg. Chem. 59 (2020) 6648–6678.
[30] Q. Poladian, B. İlhan-Ceylan, O. Bölükbaşı-Yalçınkaya, B. Türkmenoğlu, Y. Kurt, N2O2 Schiff-Base nickel(II) and iron(III) template complexes of 2-hydroxy-5-ethoxyacetophenone S-methylthiosemicarbazone: synthesis, characterization, DFT calculations, molecular docking, and antioxidant activity, Inorg. Chem. 588 (2025) 122844.
[31] S. Bakthavatsalam, A. Sarkar, A. Rakshit, S. Jain, A. Kumar, A. Datta, Tuning macrocycles to design 'turn-on'fluorescence probes for manganese (II) sensing in live cells, Chem. Commun. 51 (2015) 2605–2608.
[32] S. Rai, P.K. Singh, S. Mankotia, J. Swain, S.B. Satbhai, Iron homeostasis in plants and its crosstalk with copper, zinc, and manganese, Plant Stress 1 (2021) 100008.
[33] J. Pierre, M. Fontecave, R. Crichton, Chemistry for an essential biological process: the reduction of ferric iron, Biometals 15 (2002) 341–346.
[34] M.H. Torre, D. Gambino, J. Araujo, H. Cerecetto, M. González, M.L. Lavaggi, A. Azqueta, A.L. de Cerain, A.M. Vega, U. Abram, Novel cu(II) quinoxaline N^1, N^4-dioxide complexes as selective hypoxic cytotoxins, Eur. J. Med. Chem. 40 (2005) 473–480.
[35] P.B. Pansuriya, M. Patel, Iron(III) complexes: preparation, characterization, antibacterial activity and DNA-binding, J. Enzyme Inhib. Med. Chem. 23 (2008) 230–239.
[36] V. Balzani, V. Carassiti, L. Moggi, N. Sabbatini, Photochemistry of coordination compounds. XIV. Electron transfer and d-d excitation in cobalt(III)-amino acid complexes, Inorg. Chem. 4 (1965) 1247–1250.
[37] Schwert, D.D.; Davies, J.A.; Richardson, N. Non-gadolinium-based MRI contrast agents. In *Contrast Agents I: Magnetic Resonance Imaging*, Krause, W., Ed.; Springer Berlin Heidelberg: Berlin, Heidelberg, 2002; pp. 165–199.
[38] M. Farooq, A. Sharma, Z. Almarhoon, A. Al-Dhfyan, A. El-Faham, N.A. Taha, M. A. Wadaan, B.G. de la Torre, F. Albericio, Design and synthesis of mono-and di-pyrazolyl-*s*-triazine derivatives, their anticancer profile in human cancer cell lines, and in vivo toxicity in zebrafish embryos, Bioorg. Chem. 87 (2019) 457–464.
[39] H.H. Al-Rasheed, S.A. AL-Khamis, A. Barakat, A. El-Faham, M. Haukka, S. M. Soliman, Synthesis and characterizations of novel Isatin-*s*-Triazine Hydrazone derivatives; X-ray structure, Hirshfeld analysis and DFT calculations, Crystals 13 (2023) 305.
[40] I. Shawish, A. Barakat, A. Aldalbahi, W. Alshaer, F. Daoud, D.A. Alqudah, M. Al Zoubi, M.M.M. Hatmal, M.S. Nafie, M. Haukka, Acetic acid mediated for one-pot synthesis of novel pyrazolyl *s*-triazine derivatives for the targeted therapy of triple-negative breast tumor cells (MDA-MB-231) *via* EGFR/PI3K/AKT/mTOR signaling cascades, Pharmaceutics 14 (2022) 1558.
[41] Crysalis CCD, Oxford Diffraction Ltd: Abingdon, Oxfordshire, UK, 2005.
[42] Crysalis RED, Oxford Diffraction Ltd: Abingdon, Oxfordshire, UK, 2005.
[43] G.M. Sheldrick, Crystal structure refinement with SHELXL, Acta Crystallogr. Sect. C Struct. Chem. 71 (2015) 3–8.
[44] O.V. Dolomanov, L.J. Bourhis, R.J. Gildea, J.A.K. Howard, H. Puschmann, OLEX2: a complete structure solution, refinement and analysis program, J. Appl. Cryst. 42 (2009) 339–341.
[45] C.F. Macrae, I. Sovago, S.J. Cottrell, P.T. Galek, P. McCabe, E. Pidcock, M. Platings, G.P. Shields, J.S. Stevens, M. Towler, Mercury 4.0: from visualization to analysis, design and prediction, J. Appl. Cryst. 53 (2020) 226–235.
[46] M. Turner, J. McKinnon, S. Wolff, D. Grimwood, P. Spackman, D. Jayatilaka, M. Spackman, CrystalExplorer17, 2017.
[47] F.L. Hirshfeld, Bonded-atom fragments for describing molecular charge densities, Theor. Chim. Acta 44 (1977) 129–138.
[48] Frisch, M. Gaussian 09, Revision d. 01, Gaussian. *Inc,* Wallingford CT 2009, 201.
[49] P.J. Hay, W.R. Wadt, Ab initio effective core potentials for molecular calculations. Potentials for the transition metal atoms Sc to hg, J. Chem. Phys. 82 (1985) 270–283.
[50] T. Lu, F. Chen, Multiwfn: a multifunctional wavefunction analyzer, J. Comput. Chem. 33 (2012) 580–592.
[51] T. Mosmann, Rapid colorimetric assay for cellular growth and survival: application to proliferation and cytotoxicity assays, J. Immunol. Methods 65 (1983) 55–63.
[52] H.K. Mahmoud, H.A. Abdelhady, M.M. Elaasser, D.Z. Hassain, S.M. Gomha, Microwave-assisted one-pot three component synthesis of some thiazolyl (hydrazonoethyl) thiazoles as potential anti-breast cancer agents, Polycycl. Aromat. Compd. 42 (2022) 7232–7246.
[53] E.A. Abdelsalam, A.A. Abd El-Hafeez, W.M. Eldehna, M.A. El Hassab, H.M. M. Marzouk, M.M. Elaasser, N.A. Abou Taleb, K.M. Amin, H.A. Abdel-Aziz, P. Ghosh, Discovery of novel thiazolyl-pyrazolines as dual EGFR and VEGFR-2

inhibitors endowed with in vitro antitumor activity towards non-small lung cancer, J. Enzym. Inhib. Med. Chem. 37 (2022) 2265–2282.
[54] A.J. Rasras, R.A. Al-Qawasmeh, M. El-Naggar, I. Shehadi, M.M. Elaasser, Y.A. Al-Soud, Design, synthesis and antimicrobial assessments of aminoacetylenic-piperazine nitroimidazole hybrid compounds, Z. Naturforsch. C 78 (2023) 113–121.
[55] M.F. Abo-Ashour, W.M. Eldehna, R.F. George, M.M. Abdel-Aziz, M.M. Elaasser, N. M.A. Gawad, A. Gupta, S. Bhakta, S.M. Abou-Seri, Novel indole-thiazolidinone conjugates: design, synthesis and whole-cell phenotypic evaluation as a novel class of antimicrobial agents, Eur. J. Med. Chem. 160 (2018) 49–60.
[56] H.S. Ibrahim, W.M. Eldehna, H.A. Abdel-Aziz, M.M. Elaasser, M.M. Abdel-Aziz, Improvement of antibacterial activity of some sulfa drugs through linkage to certain phthalazin-1(2*H*)-one scaffolds, Eur. J. Med. Chem. 85 (2014) 480–486.
[57] M.M. Ghorab, M.S. Alsaid, M.S. El-Gaby, N.A. Safwat, M.M. Elaasser, A. M. Soliman, Biological evaluation of some new *N*-(2,6-dimethoxypyrimidinyl) thioureido benzenesulfonamide derivatives as potential antimicrobial and anticancer agents, Eur. J. Med. Chem. 124 (2016) 299–310.
[58] N. Heydari, R. Bikas, T. Lis, Chemical CO 2 fixation by a heterogenised Zn (II)-hydrazone complex, RSC Adv. 15 (2025) 5977–5988.
[59] R. Bikas, N. Heydari, S. Jashnsaz, T. Lis, Spectroscopic and structural studies of a Cr (III)-hydrazone complex and the effect of solvent on its selectivity in the oxidation of benzyl alcohol, J. Mol. Struct. 1340 (2025) 142528.
[60] N. Heydari, R. Bikas, M. Siczek, T. Lis, Green carbon–carbon homocoupling of terminal alkynes by a silica supported cu(II)-hydrazone coordination compound, Dalton Trans. 52 (2023) 421–433.
[61] A. Sreekanth, H.-K. Fun, M.P. Kurup, Structural and spectral studies of an iron(III) complex $[Fe(Pranthas)_2][FeCl_4]$ derived from 2-acetylpyridine-*N*(4), *N*(4)-(butane-1,4-diyl) thiosemicarbazone (HPranthas), J. Mol. Struct. 737 (2005) 61–67.
[62] A. Sreekanth, M.P. Kurup, Synthesis, EPR and Mössbauer spectral studies of new iron(III) complexes with 2-benzoylpyridine-N(4), N(4)-(butane-1,4-diyl) thiosemicarbazone (HBpypTsc): X-ray structure of $[Fe(BpypTsc)_2]$ $FeCl_4{\cdot}2H_2O$ and the free ligand, Polyhedron 23 (2004) 969–978.
[63] J.S. Sultan, E. Alsalihi, A.S. Al-Fahdawi, A.J. Jarad, New Schiff base crystal ligand type $[NO_2]$ derived from the interacting of 2-aminophenol with glyoxylic acid, and its $[N_2O_4]$ MnII complex, synthesizing and characterizing, Egypt. J. Chem. 63 (2020) 325–335.
[64] S. Yan, D.D. Cox, L.L. Pearce, C. Juarez-Garcia, L. Que Jr., J.H. Zhang, C. J. O'connor, A (μ-oxo)(μ-carboxylato) diiron(III) complex with distinct iron sites, Inorg. Chem. 28 (1989) 2507–2509.
[65] R.E. Norman, R.C. Holz, S. Ménage, C.J. O'Connor, J.H. Zhang, L. Que Jr., Studies on the mechanism of oxygen activation by iron complexes, Inorg. Chem. 29 (1990) 4629–4631.
[66] H. Zheng, Y. Zang, Y. Dong, V.G. Young, L. Que Jr., Complexes with $Fe(III)_2(\mu\text{-}O)(\mu\text{-}OH)$, $Fe(III)_2(\mu\text{-}O)_2$, and $[Fe(III)_3(\mu_2\text{-}O)_3]$ cores: structures, spectroscopy, and core interconversions, J. Am. Chem. Soc. 121 (1999) 2226–2235.
[67] P. Chábera, Y. Liu, O. Prakash, E. Thyrhaug, A. El Nahhas, A. Honarfar, L.A. Fredin, T.C.B. Harlang, K.S. Kjær, et al., A low-spin Fe(III) complex with 100-ps ligand-to-metal charge transfer photoluminescence, Nature 543 (2017) 695–699.
[68] K.S. Kjær, N. Kaul, O. Prakash, P. Chábera, N.W. Rosemann, A. Honarfar, O. Gordivska, L.A. Fredin, K.E. Bergquist, et al., Luminescence and reactivity of a charge-transfer excited iron complex with nanosecond lifetime, Science 363 (2019) 249–253.
[69] A.W. Addison, T.N. Rao, J. Reedijk, J. van Rijn, G.C. Verschoor, Synthesis, structure, and spectroscopic properties of copper(II) compounds containing nitrogen–sulfur donor ligands, J. Chem. Soc. Dalton Trans. 7 (1984) 1349–1356.
[70] A. Yousri, S.I. Gad, M.A. Abu-Youssef, A. El-Faham, A. Barakat, R. Tatikonda, M. Haukka, S.M. Soliman, Synthesis of co(II), Mn(II), and Ni(II) complexes with 4-(4, 6-*bis*(3, 5-dimethyl-1*H*-pyrazol-1-yl)-1, 3, 5-triazin-2-yl) morpholine; X-ray structure, Hirshfeld, AIM, and biological studies, Inorg. Chim. Acta 573 (2024) 122320.
[71] S.M. Soliman, H.H. Al-Rasheed, A. El-Faham, Synthesis, X-ray structure, Hirshfeld analysis of biologically active Mn(II) pincer complexes based on s-Triazine ligands, Crystals 10 (2020) 931.
[72] R. Ketkaew, Y. Tantirungrotechai, P. Harding, G. Chastanet, P. Guionneau, M. Marchivie, D.J. Harding, OctaDist: a tool for calculating distortion parameters in spin crossover and coordination complexes, Dalton Trans. 50 (2021) 1086–1096.
[73] Refaat, H.M.; Alotaibi, A.A.M.; Dege, N.; El-Faham, A.; Soliman, S.M. Syntheses, X-ray structure and biological studies of binuclear μ-oxo diiron complexes with *s*-triazine pincer ligand. Inorg. Chim. Acta 2022, 543, 121196.81.
[74] H.M. Refaat, A.A.M. Alotaibi, N. Dege, A. El-Faham, S.M. Soliman, Synthesis, structure and biological evaluations of Zn(II) pincer complexes based on *s*-triazine type chelator, Molecules 27 (2022) 3625.
[75] M. Hassan, A. El-Faham, A. Barakat, M. Haukka, R. Tatikonda, M.A.M. Abu-Youssef, S.M. Soliman, A. Yousri, Synthesis, X-ray structure, cytotoxic, and antimicrobial activities of Zn(II) complexes with a hydrazono *s*-triazine bearing pyridyl arm, Inorganics 12 (2024) 176.
[76] C. Jelsch, K. Ejsmont, L. Hudera, The enrichment ratio of atomic contacts in crystals, an indicator derived from the Hirshfeld surface analysis, IUCrJ 1 (2014) 119–128.
[77] A. Das, S. Demeshko, S. Dechert, F. Meyer, A new triazine-based tricompartmental ligand for stepwise assembly of mononuclear, dinuclear, and 1D-polymeric heptacoordinate manganese(II)/azido complexes, Eur. J. Inorg. Chem. (2011) 1240–1248.
[78] L. Cianchi, F. Giallo, M. Lantieri, P. Moretti, G. Spina, A. Caneschi, Spin dynamics of the magnetic dimer $[Fe(OMe)(dpm)_2]_2$ studied using Mössbauer spectroscopy, Phys. Rev. B 69 (2004) 014418.
[79] R.F.W. Bader, H. Essén, The characterization of atomic interactions, J. Chem. Phys. 80 (1984) 1943–1960.
[80] D. Cremer, E. Kraka, Chemical bonds without bonding electron density—does the difference electron-density analysis suffice for a description of the chemical bond? Angew. Chem. Int. Ed. Engl. 23 (1984) 627–628.
[81] D. Cremer, E. Kraka, A description of the chemical bond in terms of local properties of electron density and energy, Croat. Chem. Acta 57 (1984) 1259–1281.
[82] E. Espinosa, I. Alkorta, J. Elguero, E. Molins, From weak to strong interactions: a comprehensive analysis of the topological and energetic properties of the electron density distribution involving X–H···F–Y systems, J. Chem. Phys. 117 (2002) 5529–5542.
[83] N.S. Venkataramanan, A. Suvitha, Y. Kawazoe, Unravelling the nature of binding of cubane and substituted cubanes within cucurbiturils: a DFT and NCI study, J. Mol. Liq. 260 (2018) 18–29.
[84] E. Espinosa, E. Molins, C. Lecomte, Hydrogen bond strengths revealed by topological analyses of experimentally observed electron densities, Chem. Phys. Lett. 285 (1998) 170–173.
[85] F. Bray, M. Laversanne, H. Sung, et al., Global cancer statistics 2022: GLOBOCAN estimates of incidence and mortality worldwide for 36 cancers in 185 countries, CA Cancer J. Clin. 74 (2024) 229–263.
[86] Z.M. Kheiralla, H.H. Abo-Ghalia, M.M. Elaasser, M.F. Hemeda, S.Y. Ibrahim, Endophyte Chaetomium, Potential Bioactivity: Pharmaceutical and Phytochemical Analyses, 2023.
[87] M. Fouad, M. Elaasser, Convenient one-pot synthesis and biological evaluation of novel 3, 5-dimethyl-1*H*-pyrazole-1-carbothiohydrazide derivatives as new anti-tumor agents against both liver carcinoma (HepG2) and lung carcinoma (A549) cell lines, ChemRxiv (2023).
[88] S.M. Soliman, R.A. Massoud, H.H. Al-Rasheed, A. El-Faham, Syntheses and structural investigations of penta-coordinated co(II) complexes with *bis*-pyrazolo-*s*-triazine pincer ligands, and evaluation of their antimicrobial and antioxidant activities, Molecules 26 (2021) 3633.